Research Article

Luminescent sensing film based on sulfosalicylic acid modified Tb(III)-doped yttrium hydroxide nanosheets

Wei YANG, Qiang LI*, Xiaohong ZHENG, Xi LI, Xin LI

Department of Chemistry, East China Normal University, Shanghai 200062, China

Abstract: Sulfosalicylic acid (SSA) was used as an intercalation agent and an excellent antenna to synthesize layered rare-earth hydroxide (LRH) materials and directly obtain SSA-modified terbium-doped ytterbium hydroxide nanosheets by mechanical exfoliation. The crystal structure and morphologies of the LRHs and nanosheets were determined by X-ray diffraction, scanning electron microscopy, and transmission electron microscopy. The particle size and zeta potential of the prepared nanosheets were also analyzed. The as-prepared nanosheets exhibited excellent luminescent properties. The positively charged nanosheets were electrophoretically deposited on a conductive glass to form a thin film. The luminescence of this thin film can be quenched by chromate (CrO_4^{2-}) and bilirubin (BR), which shows good sensing properties. The quenching mechanism of the sensing film by CrO_4^{2-} and BR was discussed based on the spectra and structure of the film.

Keywords: rare-earth hydroxide; nanosheets; thin-film sensor; chromate (CrO_4^{2-}); bilirubin (BR)

1   Introduction

Lanthanides nanomaterials and complexes play an important role in inorganic chemistry and materials science, because of their unique spectral characteristics and 4f electron orbits shielded by $5s^2$ and $5p^6$ shells [1]. The lanthanide ions have a large Stokes shift and show strong, pure, long life and narrow emission bands [2]. The emitted light emission ranges from visible light region (Tb^{3+}, Eu^{3+}) to near infrared (NIR) (Nd^{3+}, Pr^{3+}, Er^{3+}) [3]. The luminescence of lanthanides has attracted great interest for use in lanthanide liquid crystal displays, electroluminescent materials, bioimaging, multiphoton excitation probes, and luminescence light-emitting devices, magnetic resonance imaging (MRI)

agents, energy conversion devices or luminescent response probes for biological testing [4].

In recent decades, a class of so-called anionic clay lamellar double hydroxides (LDHs) have gained tremendous success due to their important industrial and academic attention to physical and chemical properties. LDHs are hydrotalcite hydroxides in which the isomorphous divalent metal ion is replaced by a trivalent metal ion to produce a net positive charge [5]. The greatest characteristics of LDHs are large surface area, high anion exchange capacity, adjustable surface charge density, good composition, good heat resistance, and high stability [6]. Layered rare-earth hydroxides (LRHs) share the same advantages of LDHs [7]. Due to the unique electronic, optical, magnetic, and rare-earth elements, the catalytic properties of LRHs have attracted immediate attention since their inception, and extensive efforts in their synthesis, structural

---

* Corresponding author.
E-mail: qli@chem.ecnu.edu.cn

characterization, anion exchange, and stripping have been made [8]. LRHs may possibly be stripped into individual nanosheets to further construct a variety of nanostructures, particularly highly transparent functional films.

Chromium is a transition metal in the group VI-B of the periodic table [9]. It can have several oxidation states, but the most stable and common forms are trivalent Cr(III) and hexavalent Cr(VI), both of which show very different chemical properties [10]. Cr(VI) is generally considered to be the most toxic, such as chromate (CrO_4^{2-}) or dichromate ($Cr_2O_7^{2-}$) ions. In addition, Cr(III) can also be oxidized to Cr(VI) in the presence of excess oxygen and converted into a more toxic form Cr(VI). CrO_4^{2-} is a common toxic anion that can accumulate in organisms, causing liver disease, gene mutations, malformations, and cancer [11]. The detection of the presence of low chromate concentration is the direction in which remediation efforts are essential to identify contaminated sites and control areas. Analytical methods such as inductively coupled plasma atomic electron spectroscopy (ICP/AES) or mass spectrometry (ICP/MS), flow injection atomic absorption (FIAAS), or electrochemical methods are the most commonly used methods for quantifying the total metal content [12]. These methods require strong acid for sample processing, which is a strong acid contaminant, and does not distinguish between bioavailable and non-biologically useful metals. Therefore, it is difficult to predict the environmental risks of each metal using these methods. In order to better purify and protect our water resources, it will be necessary to detect the CrO_4^{2-} in an efficient and low-cost way. In addition, it is important to identify and monitor CrO_4^{2-} by direct visual inspection, for example by developing suitable luminescence sensors.

Bilirubin (BR) is a common hemoglobin metabolite that is usually combined with albumin to form a water-soluble complex [13]. Serum BR levels can be used to assess liver function and identify liver diseases such as cirrhosis, acute or chronic hepatitis, cholestasis, primary cancer, hemolytic anemia, and pancreatic cancer [14]. Moreover, abnormal metabolism of BR, especially in newborns, may cause jaundice [15]. In the past few years, a number of BR detection methods have been developed, including those based on enzymatic assays, fluorescence, capillary electrophoresis, high-performance liquid chromatography, chemiluminescence, and piezoelectricity [16,17]. However, during this progress,

most BR sensors are complex, costly to operate, and detect BR in an indirect way, which implies that the search for new materials and methods to improve BR sensor sensitivity, selectivity, and stability is still ongoing.

Herein, we prepared Tb(III)-doped Y hydroxide nanosheets to fabricate a rare-earth luminescence sensor, using sulfosalicylic acid (SSA) as intercalation agent and ligand for the one-step synthesis and modification of rare-earth nanosheets. The above nanosheets were processed by electrophoretic deposition into a luminescent thin film to afford a CrO_4^{2-} and BR sensor.

2 Materials and methods

2. 1 Preparation of the sensing film

Solutions of Tb(NO$_3$)$_3$ (5×10^{-4} M, 1.58 mL) and Y(NO$_3$)$_3$ (5×10^{-4} M, 30 mL) were mixed, and the pH of the mixture was adjusted to 6–7 by dilute aqueous ammonia. SSA was neutralized by aqueous NaOH to pH = 6–7, and 10 mL of the obtained solution (1.8×10^{-3} M) was added to the above Tb/Y solution. The resulting mixture was loaded into a hydrothermal reactor and incubated at 120 ℃ for 24 h after 0.5 h stirring. After 24 h, the hydrothermal reactor was automatically cooled, and the solid product was separated by filtration, sequentially washed with deionized water and anhydrous ethanol, and dried at 60 ℃ to afford SSA-intercalated Tb^{3+}-doped Y hydroxide nanosheets. The layered structure of the thus obtained LRH was validated by X-ray diffraction (XRD; D8 Advance, Bruker AXS Co., Ltd., Germany), and the morphologies of Tb^{3+}-doped Y nitrate hydroxide and SSA-intercalated Tb^{3+}-doped Y hydroxide were verified by cold-field-emission scanning electron microscopy (SEM; S-4800, Hitachi, Japan) and transmission electron microscopy (TEM; JEM2100, Hitachi, Japan). LRHs intercalated by nitrate were also synthesized in similar method, and compared with LRHs intercalated by SSA.

Starting from as-obtained LRHs, rare-earth nanosheet sol was obtained by ultrasonic ablation in n-butanol for 40 min. Morphology of nanosheets was determined by a JEM2100 transmission electron microscope (Hitachi, Japan). The particle size and zeta potential prepared nanosheets were analyzed by NANO ZS3600 nanoparticle size and zeta potential analyzer.

Rare-earth nanosheets were deposited onto conductive glass (ITO) by electrophoretic deposition. In order to

enhance the stability of the film of nanosheets, as-prepared film was coated with polystyrene by Czochralski method [18]. The surface hydrophobicity of the thus produced sensing film was checked by infiltration angle measurements, and its luminescent properties were probed by fluorescence measurements.

2. 2 Sensing properties of thin film of nanosheets

Firstly the sensing properties of CrO_4^{2-} based on the thin film of nanosheets were investigated. Solutions of CrO_4^{2-} (0–100 M) were prepared by dissolving appropriate amounts of $K_2Cr_2O_7$ in distilled water. In view of the very low concentration and close-to-neutral pH of the above solutions, $Cr_2O_7^{2-}$ ions were completely converted to CrO_4^{2-}. Sample probes of equal volume but different concentrations were placed onto the sensor, and luminescence intensity changes were recorded using a fluorescence spectrometer. The relationship between the luminous intensity of the sensing film and CrO_4^{2-} concentration was described by the Stern–Volmer equation, $I_0/I = 1 + K_{SV}[CrO_4^{2-}]$ [19, 20], where I_0 and I are luminescence intensities in the absence and presence of CrO_4^{2-}, respectively. The mechanism of CrO_4^{2-}-induced luminescence quenching was studied using an Agilent Cary UV-8000 spectrophotometer (Timme, China).

Then the sensing properties of BR based on the thin film of nanosheets were determined. BR solutions (0–100 M) were prepared by dissolving appropriate BR amounts in 2 mL of BR-free serum, as reported previously [21–23]. Aliquots (50 L) of the prepared BR solutions were placed on the sensor surface, and luminous intensity changes were measured as described above. Absorption spectra of nanosheets, nanosheets-BR, SSA, SSA-BR, BR were also tested and compared.

3 Results and discussion

3. 1 Nanosheet and sensing film properties

The spacing of rare-earth hydroxide layers could be effectively changed by varying the size of intercalated molecules. Usually, starting from nitrate hydroxides, some organic compounds were employed to replace interlayer nitrate to enlarge the interlayer spacing [24–26]. Here a more efficient method was developed. LRHs with SSA as intercalation can be directly synthesized by hydrothermal reaction. Because SSA is larger than nitrate, SSA as an intercalation agent instead of nitrate can increase the interlayer spacing of LRHs. In Fig. 1, when nitrates between layers are replaced by SSA, the interlayer spacing expands from 9.2 to 11.6 Å. The reason why the interlayer spacing is 11.6 Å is that the negatively-charged sulfo group in SSA is easily in close proximity with the positively-charged LRHs. Furthermore, the carboxylic acid in SSA coordinates with LRHs, resulting in the oblique insertion of SSA into the nanosheets instead of vertical insertion. This phenomenon that intercalation ions are not inserted vertically has been reported in many literatures [27–29]. By changing the size of the intercalated layer molecules, the spacing of rare-earth hydroxide layers can be effectively changed. The above results show that SSA replaces nitrate between layered material and the layer spacing is successfully supported.

Figure 2(a) shows a representative SEM image of Tb^{3+}-doped Y nitrate hydroxide nanosheets, revealing that this material has a layered structure with a small interlayer spacing, which resultes in a block-shape appearance. Figure 2(b) shows a representative SEM image of SSA-intercalated hydroxide nanosheets, demonstrating the onset of bulk material bending and
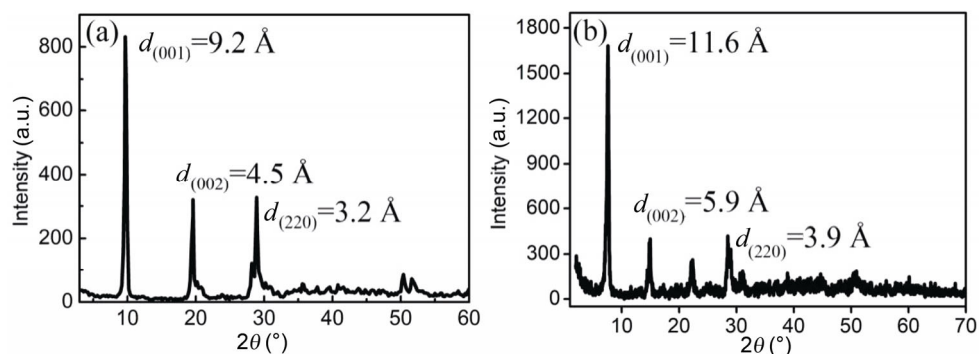
Fig. 1 XRD patterns of (a) Tb^{3+}-doped Y nitrate hydroxide and (b) SSA-intercalated Tb^{3+}-doped Y hydroxide.

the appearance of numerous folds. The increased layer spacing caused by SSA intercalation decreases the attraction between layers and hence facilitates stripping to afford individual nanosheets, the size and thickness of which were determined by TEM. Figure 2(c) shows a TEM image of nanosheets obtained by sonicating SSA-intercalated Tb^{3+}-doped Y hydroxide in *n*-butanol for 40 min, revealing that the obtained nanosheets are very thin and relatively uniform in shape and size. Thus, SEM and TEM imaging confirms that the one-step synthesis of nanosheets is successful. The monolayer nanosheets as shown in Fig. 3 are around 3 nm. When two nanosheets are stacked, their thickness is exactly twice that of one layer. Because of the solid intercalation product, SSA is inserted obliquely, while in AFM the nanoplatelets are dispersed in the organic solution. Due to the solvation of SSA, the structure spreads out, and the upper and lower surfaces of the nanosheets are both coordinated by the SSA. The thickness of nanosheets is larger than that obtained by XRD.

As-prepared nanosheets were also characterized by NANO ZS3600. Figure 4(a) shows that the nanosheet size is evenly distributed around 279 nm, in accordance with Fig. 2(c), and the obtained nanosheet zeta potential of +39.7 mV (Fig. 4(b)) implies that the corresponding sensor film could be obtained at the cathode by electrophoretic deposition.

A thin film can be easily prepared from nanosheets by electrophoretic deposition on ITO glass. However, stability of this thin film might be deeply influenced by aqueous solution. So this thin film was modified by polystyrene (PS). Figure 5(a) shows the infiltration angles obtained for glass coated with nanosheets and nanosheets+3wt%PS, demonstrating that the deposition of modified nanosheets increases surface
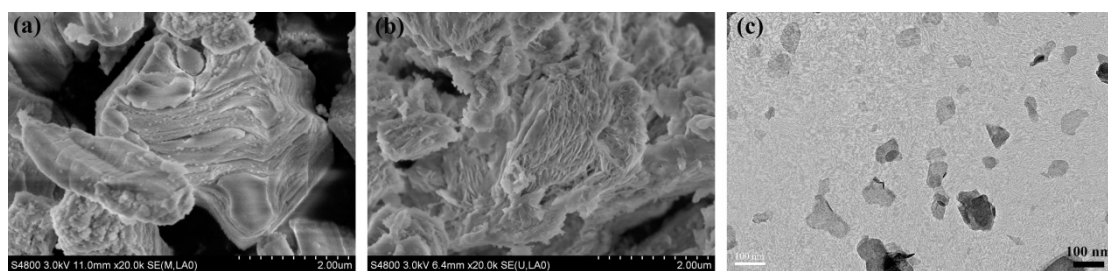

Fig. 2 SEM images of (a) layered Tb^{3+}-doped Y nitrate hydroxide and (b) SSA-intercalated layered Tb^{3+}-doped Y hydroxide. (c) TEM image of the exfoliated product obtained after SSA intercalation.
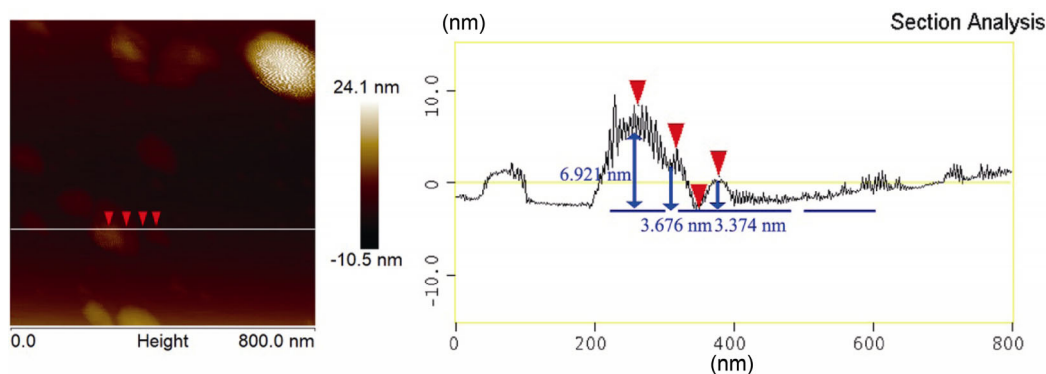

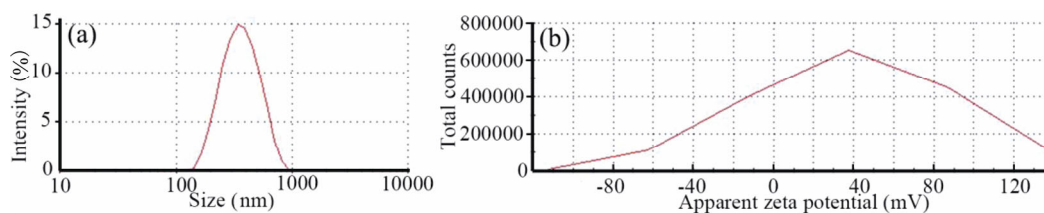**Fig. 3** AFM images of SSA-intercalated layered Tb^{3+}-doped Y nanosheets.

Fig. 4 (a) Malvern particle size distribution and (b) zeta potential of nanosheets.

Fig. 5 (a) Infiltration angle measurements performed for blank glass, nanosheet-coated glass, and glass coated with nanosheets +3wt%PS (α=45°, β=65°, γ=90°); (b) the sensing film.

hydrophobicity (β=65°), with a further increase observed after PS wrapping (γ=90°). Therefore, PS-encapsulated rare-earth nanosheets are concluded to be well suited for the fabrication of easy-to-carry sensors preserving the original nanosheet characteristics in aqueous media. As shown in Fig. 5(b), the obtained sensing film has good light transmittance and is quite uniform. The thickness of the film is 24 μm detected by an ellipsometer.

The excitation spectrum of the sensing film (Fig. 6(a)) features maximum at 263 nm corresponding to spin-allowed Tb–O charge transfer in Tb(III). Notably, in addition to acting as an intercalation agent, SSA can effectively absorb energy at 351 nm and transmit it to the luminescent center, which gives rise to the so-called "antenna effect" [30]. Figure 6(b) shows the emission spectrum of the sensing film, revealing the

presence of maxima at 484, 544, 583, and 622 nm corresponding to the $^5D_4 \rightarrow {}^7F_J$ transitions of Tb^{3+} (J = 6–3) [31].

3. 2   Response of the sensing film to CrO_4^{2-}

Firstly, the CrO_4^{2-} sensing based on as-prepared luminescence film was studied. Figure 7(a) shows the emission spectra of the sensing film at different CrO_4^{2-} concentrations, revealing that its luminescent intensity is reduced with increasing analyte concentration (0–100 M) and hence indicating that the above anion quenches the luminescence of SSA-modified nanosheets. In a homogeneous medium, luminescence quenching can be modeled using the above mentioned Stern–Volmer equation, the application of which to this case showes that luminescence intensity is linearly dependent on CrO_4^{2-} concentration, with the corresponding
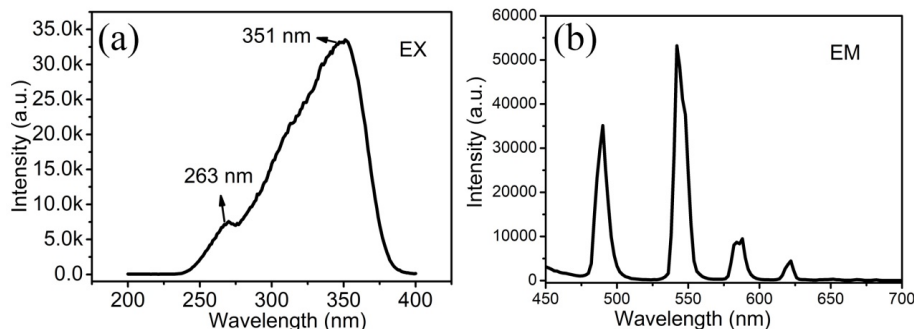

Fig. 6   (a) Excitation and (b) emission spectra of the sensing film.
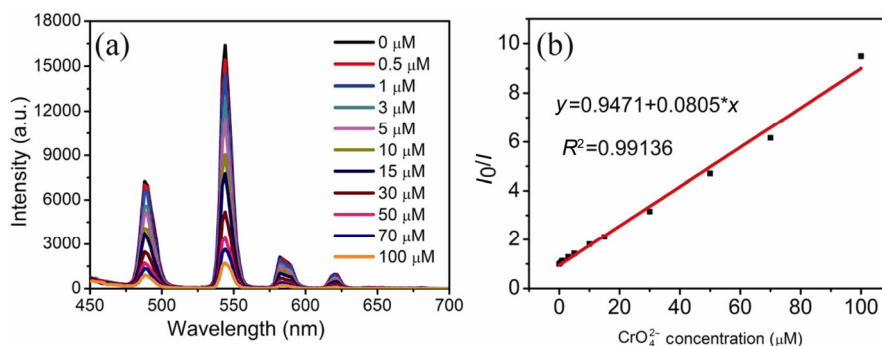

Fig. 7   (a) Emission spectra of the sensing film recorded at different CrO_4^{2-} concentrations. (b) Relationship between the luminescence intensity of the sensing film and the concentration of CrO_4^{2-}.
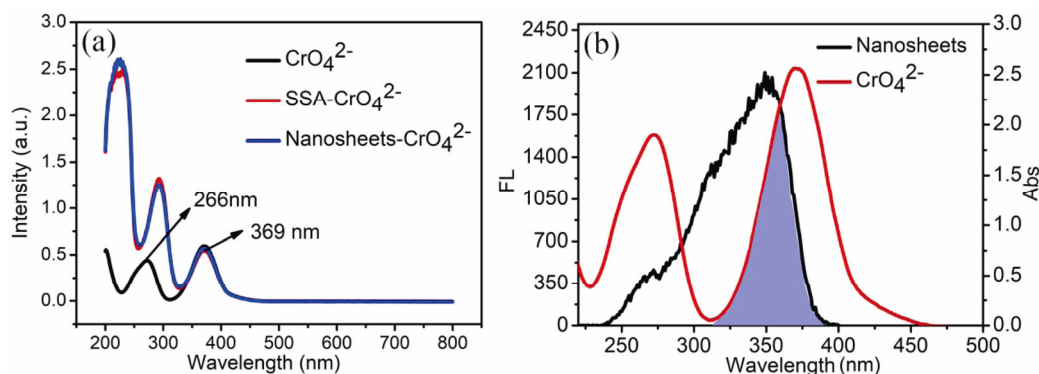
Fig. 8 (a) Absorption spectra of CrO_4^{2-}, SSA-CrO_4^{2-}, and nanosheets-CrO_4^{2-}. (b) Overlap of the SSA-intercalated nanosheet excitation spectrum with the absorption spectrum of CrO_4^{2-}.

slope equaling 0.0805 and the correlation coefficient (R^2) equaling 0.99136 (Fig. 7(b)). Although fluorescent rare-earth and transition metal complexes are widely used as probes for the detection of CrO_4^{2-}, the sensing film described herein exhibits the highest quenching efficiency reported so far [12,31–33]. Additionally, the detection range of the developed method is wider than those obtained for $Eu_2(tpbpc)_4CO_3 \cdot 4H_2O$ (0.0–0.3 M) [34] and EuMOF (0.0–2.6 M) [4] probes. Therefore, all above mentioned results indicate that the as-prepared sensor is well suited for CrO_4^{2-} detection and exhibits a range of potential industrial applications, such as being easy to preserve, transport, and use.

The mechanism of CrO_4^{2-}-induced luminescence quenching was determined by UV and fluorescence spectroscopy. Figure 8(a) shows the absorption spectra of CrO_4^{2-}, SSA-CrO_4^{2-}, and nanosheets-CrO_4^{2-}, revealing the presence of peaks at 266 and 369 nm attributed to bands II and I of CrO_4^{2-}, respectively [35]. The band at 369 nm is associated with Cr–O vibration accompanying the $O^{2-} \rightarrow Cr(VI)$ charge transfer (ligand-to-metal charge transfer, LMCT) [36]. Notably, mixing of CrO_4^{2-} with nanosheets does not result in any significant shift of the two absorption maxima or cause the appearance of new peaks, which illustrates the absence of coordination interactions between CrO_4^{2-} and SSA/nanosheets. Figure 8(b) shows that the nanosheet excitation peak is located at 351 nm, which is attributed to the contribution of the SSA ligand. Simultaneously, the maximum absorption peak of CrO_4^{2-} is observed at 369 nm and thus significantly overlapped with the nanosheet excitation peak. According to the antenna effect, the energy absorbed by SSA at 351 nm is well matched with the absorption energy of CrO_4^{2-} (369 nm) and is therefore partially transferred to the latter anion, which decreases the amount of energy received by the

luminescent center and causes luminescence quenching. Spin-allowed LMCT is well known to exhibit high transition and conversion efficiencies. As shown in Fig. 9, the good energy match mentioned above allows CrO_4^{2-} to effectively interfere with the antenna effect of SSA and reduce the luminous intensity of nanosheets.

3.3 Response of the sensing film to BR

The prepared sensing film was also used for the detection of blood breakdown BR. As shown in Fig. 10(a). Notably, the luminescence intensity decreases with increasing BR concentration, and the corresponding process could be expressed as follows [37,38]:

$$[C] + n[Q] \rightarrow [C-nQ] \ (C = \text{nanosheets}; \ Q = \text{BR}) \ (1)$$

$$K_A = \frac{[C-nQ]}{[C][Q]^n} = \frac{[C_0]-[C]}{[C][Q]^n} \quad (2)$$

$$\lg \frac{F_0-F}{F} = \lg K_A + n \lg [Q] \quad (3)$$

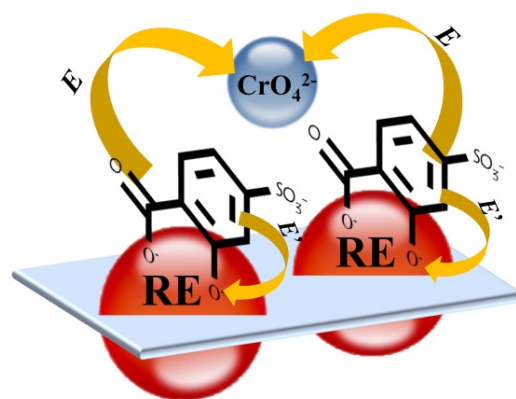where C and C_0 represent the sensing film with and

Fig. 9 Mechanism of CrO_4^{2-}-induced luminescence quenching.

without BR, respectively, and F and F_0 are the corresponding luminescence intensities, respectively.

The dependence of luminescence intensity on BR concentration was modeled according to Eq. (3), and a straight line with a slope of 0.99976 and a correlation coefficient of $R^2 = 0.92323$ is obtained (Fig. 10(b)). Because BR has coordinated with rare-earth nanosheets, the BR sensing property of nanosheets is seriously influenced by the number of layers. Usually nanosheets with single layer have highest sensing properties. The nanosheets with different layer influence the accuracy of the linear law. Most of the previously reported BR fluorescent probes or sensors are based on fluorescent proteins [39], metal organic frameworks (MOFs) [40], quantum dots [38], and rare-earth complexes [42]. The use of fluorescent proteins offers the advantages of a broad detection range and good linearity, but imposes strict preparation and storage requirements and incurs higher costs than other methods. Similarly, although MOF-based methods offer a suitable detection range and high detection sensitivity, the process of MOF preparation is very complex and thus difficult to apply in practical production. Metal complexes such as $Ru(bipy)_3^{2+}$ [43] and yttrium–norfloxacin [42] can also

be used for BR detection but do not provide a suitable detection range and are unstable. Finally, the use of S- and N-doped carbon dots allows quick and efficient BR quantitation, but the corresponding detection range is far below that of normal human BR concentrations. Therefore, the present method exhibits the advantages of sensor preparation simplicity and wide detection range. Compared to metal complexes, nanosheets exhibit increased solution-phase stability, and the nanosheet sensor film is easy to transport, allowing for convenient and fast BR detection.

Figure 11(a) shows the UV spectra of nanosheets, nanosheets-BR, SSA, SSA-BR, and BR, revealing that the position of the BR absorption peak (440 nm) is not affected by the presence of SSA, which indicates the absence of BR–SSA coordination. However, the above peak shifts from 440 to 411 nm after mixing with nanosheets, in agreement with the known ability of BR to coordinate rare-earth ions [44–46]. The emission peak of SSA located at 402 nm [47,48] significantly overlaps with the absorption peak of coordinated BR (411 nm), which results in luminescence quenching. As shown in Fig. 11(b), SSA absorbs energy to afford a singlet excited state (S_1) that is converted to the triplet
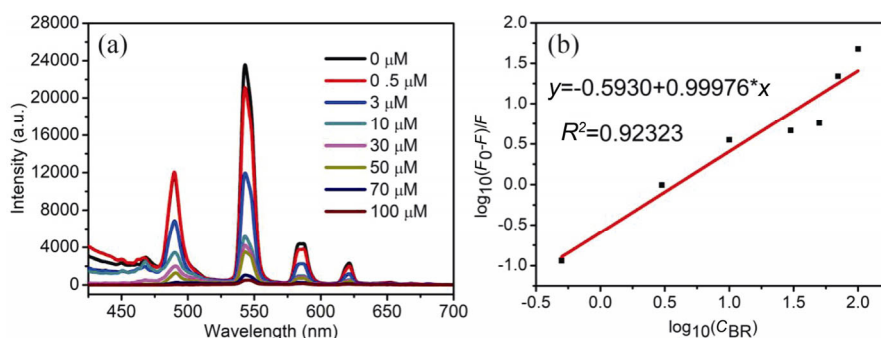

Fig. 10 (a) Luminescence emission spectra of the sensing film in presence of BR (0–100 μM). (b) Plot of lg[($F_0 - F$)/F] as a function of lg[BR].
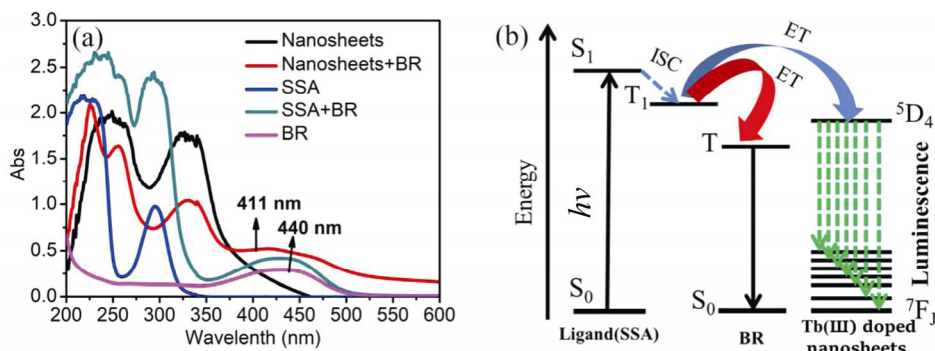

Fig. 11 (a) Absorption spectra of nanosheets, nanosheets-BR, SSA, SSA-BR, and BR. (b) Energy levels of SSA, BR, and the Tb(III) luminescence center.

Table 1 Long time stability and cycling stability

X	Y	0 Day	7 Days	30 Days	RSD (%)
CrO_4^{2-}(0.5 M)	I_0/I	0.99409	1.02881	0.9771	2.64
BR (0.5 M)	$lg[(F_0-F)/F]$	−1.2116	−1.2001	−1.1825	1.47

state (T_1) via intersystem crossing. Subsequently, energy is transferred to the nanosheet emission center (Tb^{3+}) to afford a $^5D_4$ excited state. The coordination of BR to rare-earth nanosheets and the good match between the energy of BR absorption to the energy of SSA emission allow the energy absorbed by SSA to be partially transferred to non-illuminated BR, resulting in a decrease of the nanosheet luminescence intensity.

The stability and cyclicity of the sensing film can be seen by detecting the deviations of the same concentration CrO_4^{2-} and BR in different time periods. As shown in Table 1, within a month, the long time stability and cycling stability of the sensing film are excellent.

4 Conclusions

LRHs were synthesized using SSA as an intercalation agent in a single step, and Tb(III)-doped yttrium hydroxide luminescent nanosheets modified by SSA as an excellent antenna were easily and directly produced via the exfoliation process. The resulting nanosheets were electrophoretically deposited on a conductive glass and wrapped with a PS film to prepare a thin film sensor. The luminescence properties of the sensing film revealed the efficient antenna effect of SSA on the Tb(III)-doped rare-earth nanosheets, and the sensing film could accurately and efficiently detect heavy metal ions such as CrO_4^{2-} and the breakdown of blood into BR. Both chromate and BR quenched the emission of the sensing film by interfering with the antenna effect of SSA to the luminescent center. Combined with fiber optic technology, the sensing film might be useful in environmental monitoring and medical testing.

References

[1] Zhu Q, Wang X, Li J-G. Recent progress in layered rare-earth hydroxide (LRH) and its application in luminescence. *J Adv Ceram* 2017, **6**: 177–186.

[2] Upasani M. Synthesis of $Y_3Al_5O_{12}$:Eu and $Y_3Al_5O_{12}$:Eu,Si phosphors by combustion method: Comparative investigations on the structural and spectral properties. *J Adv Ceram* 2016, **5**: 344–355.

[3] Lia X, Li J, Li J, *et al*. Upconversion $32Nb_2O_5$–$10La_2O_3$–$16ZrO_2$ glass activated with Er^{3+}/Yb^{3+} and dye sensitized solar cell application. *J Adv Ceram* 2017, **6**: 312–319.

[4] Yildirim S, Demirci S, Ertekin K, *et al*. Production, characterization, and luminescent properties of Eu^{3+} doped yttrium niobate-tantalate films. *J Adv Ceram* 2017, **6**: 33–42.

[5] Sousa R, Jouin J, Masson O, *et al*. Structure and analgesic properties of layered double hydroxides intercalated with low amounts of ibuprofen. *J Am Ceram Soc* 2017, **100**: 2712–2721.

[6] Zhang Y, Liu X, Zhang C, *et al*. Interlayer structures and dynamics of arsenate and arsenite intercalated layered double hydroxides: A first principles study. *Minerals* 2017, **7**: 53.

[7] Wang S, Shi W, Lu C. Chemisorbed oxygen on the surface of catalyst-improved cataluminescence selectivity. *Anal Chem* 2016, **88**: 4987–4994.

[8] Zhu Q, Zhang X, Li J-G, *et al*. Oriented and yellow-emitting nano-phosphor films of high transparency assembled from exfoliated nanosheets of layered rare-earth hydroxide (LRH). *J Nanosci Nanotechnol* 2017, **17**: 2471–2477.

[9] Anyanwu CU, Ezaka E. Growth responses of chromium (vi) tolerant bacteria to different concentrations of chromium. *International Journal of Basic & Applied Sciences* 2011, **11**: 41–44.

[10] Rajyalaxmi K, Merugu R, Girisham S, *et al*. Chromate reduction by purple non sulphur phototrophic bacterium *Rhodobacter* sp. GSKRLMBKU–03 isolated from pond water. *Proc Natl Acad Sci India Sect B Biol Sci* 2017, **7**: 1–7.

[11] Khonkayan K, Sansuk S, Srijaranai S, *et al*. New approach for detection of chromate ion by preconcentration with mixed metal hydroxide coupled with fluorescence sensing of copper nanoclusters. *Microchim Acta* 2017, **184**: 2965–2974.

[12] Liu W, Wang Y, Bai Z, *et al*. Hydrolytically stable luminescent cationic metal organic framework for highly sensitive and selective sensing of chromate anion in natural water systems. *ACS Appl Mater Interfaces* 2017, **9**: 16448–16457.

[13] Ziberna L, Martelanc M, Franko, *et al*. Bilirubin is an

endogenous antioxidant in human vascular endothelial cells. *Sci Rep* 2016, **6**: 29240.

[14] Bakrania B, Toit EFD, Wagner K-H, *et al*. Pre- or post-ischemic bilirubin ditaurate treatment reduces oxidative tissue damage and improves cardiac function. *Int J Cardiol* 2016, **202**: 27–33.

[15] Pahuja M, Dhawan S, Chaudhary SR. Correlation of cord blood bilirubin and neonatal hyperbilirubinemia in healthy newborns. *International Journal of Contemporary Pediatrics* 2016, **3**: 926–930.

[16] Bertini G, Pratesi S, Cosenza E, *et al*. Transcutaneous bilirubin measurement: Evaluation of Bilitest™. *Neonatology* 2008, **93**: 101–105.

[17] Chimhini GLT, Chimhuya S, Chikwasha V. Evaluation of transcutaneous bilirubinometer (DRAEGER JM 103) use in Zimbabwean newborn babies. *Maternal Health, Neonatology and Perinatology* 2018, **4**: 1–7.

[18] Galazka Z, Uecker R, Klimm D, *et al*. Scaling-up of bulk β-Ga$_2$O$_3$ single crystals by the Czochralski method. *ECS J Solid State Sci Technol* 2017, **6**: Q3007–Q3011

[19] Koley S, Panda MR, Ghosh S. Study of diffusion-assisted bimolecular electron transfer reactions: CdSe/ZnS core–shell quantum dot acts as an efficient electron donor and acceptor. *J Phys Chem C* 2016, **120**: 13456–13465.

[20] Bolattin MB, Nandibewoor ST, Joshi SD, *et al*. Interaction of hydralazine with human serum albumin and effect of β-cyclodextrin on binding: Insights from spectroscopic and molecular docking techniques. *Ind Eng Chem Res* 2016, **55**: 5454–5464.

[21] Santhosh M, Chinnadayyala SR, Kakoti A, *et al*. Selective and sensitive detection of free bilirubin in blood serum using human serum albumin stabilized gold nanoclusters as fluorometric and colorimetric probe, *Biosens Bioelectron* 2014, **59**: 370–376.

[22] Martelanc M, Žiberna L, Passamonti S, *et al*. Direct determination of free bilirubin in serum at sub-nanomolar levels. *Anal Chim Acta* 2014, **809**: 174–182.

[23] Huber AH, Zhu B, Kwan T, *et al*. Fluorescence sensor for the quantification of unbound bilirubin concentrations. *Clin Chem* 2012, **58**: 869–876.

[24] Geng F, Xin H, Matsushita Y, *et al*. New layered rare-earth hydroxides with anion-exchange properties. *Chem-Eur J* 2008, **14**: 9255–9260.

[25] Geng F, Matsushita Y, Ma R, *et al*. General synthesis and structural evolution of a layered family of Ln$_8$(OH)$_{20}$C$_{14}$·nH$_2$O (Ln = Nd, Sm, Eu, Gd, Tb, Dy, Ho, Er, Tm, and Y). *J Am Chem Soc* 2008, **130**: 16344–16350.

[26] Wu X, Liu W, Li J-G, *et al*. Sulfate exchange of the nitrate-type layered hydroxide nanosheets of Ln$_2$(OH)$_5$NO$_3$·nH$_2$O for better dispersed and multi-color luminescent Ln$_2$O$_3$ nanophosphors (Ln = Y$_{0.98}$RE$_{0.02}$,

RE = Pr, Sm, Eu, Tb, Dy, Ho, Er, and Tm). *Nanoscale Res Lett* 2016, **11**: 328–338.

[27] Zhang L, Jiang D, Xia J, *et al*. Novel luminescent yttrium oxide nanosheets doped with Eu^{3+} and Tb^{3+}. *RSC Adv* 2014, **4**: 17648–17652.

[28] Iyi N, Fujii K, Okamoto K, *et al*. Factors influencing the hydration of layered double hydroxides (LDHs) and the appearance of an intermediate second staging phase. *Appl Clay Sci* 2007, **35**: 218–227.

[29] Hu L, Ma R, Ozawa TC, *et al*. Synthesis of a solid solution series of layered Eu$_x$Gd$_{1−x}$(OH)$_{2.5}$Cl$_{0.5}$·0.9H$_2$O and its transformation into (Eu$_x$Gd$_{1−x}$)$_2$O$_3$ with enhanced photoluminescence properties. *Inorg Chem* 2010, **49**: 2960–2968.

[30] Liu Y, Li Z-W, Bao N, *et al*. Preparation and luminescent properties of (Tb^{3+}-Yb^{3+})SSA/(SBA-15) composite materials. *J Lumin* 2016, **180**: 38–45.

[31] Feng L, Bian L, Ren W, *et al*. Cooperative upconversion of Tb^{3+}/Yb^{3+}-codoped oxyfluoride glasses. *Mater Res Bull* 2017, **89**: 263–266.

[32] Song T-Q, Dong J, Gao H-L, *et al*. A unique zinc-organic framework constructed through *in situ* ligand synthesis for conversion of CO$_2$ under mild conditions and as a luminescence sensor for Cr$_2$O$_7^{2−}$/CrO$_4^{2−}$. *Dalton Trans* 2017, **46**: 13862–13868.

[33] Liu J, Ji G, Xiao J, *et al*. Ultrastable 1D europium complex for simultaneous and quantitative sensing of Cr(III) and Cr(VI) ions in aqueous solution with high selectivity and sensitivity. *Inorg Chem* 2017, **56**: 4197–4205.

[34] Li N, Zhu Q-E, Hu H-M, *et al*. Hydrothermal syntheses, crystal structures and luminescence properties of zinc(II) coordination polymers constructed by bifunctional 4′-(4-carboxyphenyl)-3,2′:6′,3″-terpyridine. *Polyhedron* 2013, **49**: 207–215.

[35] Campani E, Ferri F, Gorini G, *et al*. Resonance Raman excitation profile for the 848 cm$^{−1}$ totally symmetric mode of the chromate ion. *Chem Phys Lett* 1984, **107**: 91–95.

[36] Viti C, Marchi E, Decorosi F, *et al*. Molecular mechanisms of Cr(VI) resistance in bacteria and fungi. *FEMS Microbiol Rev* 2014, **38**: 633–659.

[37] Correa RS, Oliveira KM, Pérez H, *et al*. *cis-bis*(N-benzoyl-N′,N′-dibenzylthioureido)platinum(II): Synthesis, molecular structure and its interaction with human and bovine serum albumin. *Arabian J Chem* 2015, http://dx.doi.org/10.1016/j.arabjc.2015.10.006.

[38] Roy AS, Ghosh P, Dasgupta S. Glycation of human serum albumin affects its binding affinity towards (−)-epigallocatechin gallate. *J Incl Phenom Macrocycl Chem* 2016, **85**: 193–202.

[39] Iwatani S, Nakamura H, Kurokawa D, *et al*. Fluorescent protein-based detection of unconjugated bilirubin in

newborn serum. *Sci Rep* 2016, **6**: 28489–28496.

[40] Du Y, Li X, Lv X, *et al*. Highly sensitive and selective sensing of free bilirubin using metal-organic frameworks-based energy transfer process. *ACS Appl Mater Interfaces* 2017, **9**: 30925–30932.

[41] Anjana RR, Devi JSA, Jayasree M, *et al*. S,N-doped carbon dots as a fluorescent probe for bilirubin. *Microchim Acta* 2018, **185**: 11.

[42] Kamruzzaman M, Alam A-M, Sang HL, *et al*. Spectrofluorimetric quantification of bilirubin using yttrium–norfloxacin complex as a fluorescence probe in serum samples. *J Lumin* 2012, **132**: 3053–3057.

[43] Wabaidur SM, Eldesoky GE, Alothman ZA. The fluorescence quenching of Ru(bipy)$_3^{2+}$: An application for the determination of bilirubin in biological samples. *Luminescence* 2018, **33**: 625–629.

[44] Kuenzle CC, Pelloni RR, Weibel MH, *et al*. A proposed novel structure for the metal chelates of bilirubin. *Biochem J* 1972, **130**: 1147–1150.

[45] Velapoldi RA, Menis O. Formationand stabilities of free bilirubin and bilirubin complexes with transition and rare-earth elements. *Clin Chem* 1971, **17**: 1165–1170.

[46] Zhuang Q-K, Dai H-C, Liu H. Electrochemical study on the interaction of bilirubin with europium ions in aqueous media. *Electroanalysis* 1999, **11**: 1368–1371.

[47] Wei YJ, Li N, Qin SJ. Fluorescence spectra and fluorescence quantum yield of sulfosalicylic acid. *Spectroscopy & Spectral Analysis* 2004, **24**: 647–651. (in Chinese)

[48] Zhang J, Wang J, Wang S, *et al*. Fluorescence spectra of 5-sulfosalicylic acid at different pH values. *Ningxia Engineering Technology* 2011, **4**: 011.